RSC Advances

PAPER

View Article Online
View Journal | View Issue

Cite this: *RSC Adv.*, 2026, **16**, 5501

Enhancement of the heterogeneous photo-Fenton performance of GO/MIL-100(Fe)@Fe_3O_4 heterostructures for erythromycin degradation through accelerating Fe(II) generation

Lian Yu, *[a] Baozi Lu,[a] Zhen Liang,[b] Dabin Wang,[c] Jiarui Lu,[a] Fengyi Wei[a] and Cunzhen Liang[a]

The slow rate of the Fe^{3+}/Fe^{2+} cycle has decreased the efficiency of photo-Fenton technology for wastewater treatment. Here, a novel GO/MIL-100(Fe)@Fe_3O_4 heterostructure was constructed by growing Fe_3O_4 nanoparticles and MIL-100(Fe) onto GO, thus accelerating the Fe^{3+}/Fe^{2+} cycle and improving catalytic activity, and it was used as a heterogeneous photo-Fenton catalyst for ERY degradation. The catalyst was fully characterized by TEM, XRD, Raman spectroscopy, XPS, N_2 adsorption–desorption and UV-vis DRS. The influences of initial solution pH, H_2O_2 concentration and catalyst dosage on ERY degradation were investigated. Under optimal conditions (initial pH of 4.03, 10.0 mM H_2O_2, 0.1 g L^{-1} catalyst), the GO/MIL-100(Fe)@Fe_3O_4 + H_2O_2 + vis system removed 97.3% of ERY (0.1 mmol L^{-1}) within 60 min, and the pseudo-first-order rate constant was 0.0575 min^{-1}. Furthermore, the catalyst showed favorable stability, maintaining excellent catalytic activity even after 4 cycles. A possible degradation mechanism of ERY was proposed based on the results of characterization, ERY degradation, and reactive species analysis. Fe_3O_4, MIL-100(Fe) and GO in the catalyst showed synergistic effects; the photo-induced electrons from MIL-100(Fe) could be immediately transferred to Fe_3O_4, promoting Fe^{3+} reduction to Fe^{2+} in the photo-Fenton reaction. GO in the catalyst could promote electron transfer from MIL-100(Fe) and organics to Fe_3O_4, significantly promoting the Fe^{3+}/Fe^{2+} cycle.

Received 13th September 2025
Accepted 6th November 2025

DOI: 10.1039/d5ra06917c

rsc.li/rsc-advances

1. Introduction

Erythromycin (ERY) is usually used when people are allergic to penicillin, and it can exist in the natural environment for a long time with antibiotic activity, which may ultimately threaten human health.[1] ERY can be degraded *via* the biliary and renal tract by the human body, but undecomposed ERY enters the environment with excretion. However, more than 60% of ERY in the environment is maintained unchanged because of its chemical stability, and it has been detected in various environments.[2] The United States Environmental Protection Agency added ERY into its Contaminant Candidate List 3, while the European Union regards ERY as a high-risk priority pollutant.[3] In China, ERY has been identified as a precedence-controlled pollutant because of its frequent detection in water sources, natural waters, underground waters and wastewater treatment plants.[4]

To date, various methods have been used to remove ERY from wastewater: advanced oxidation,[5] membrane separation,[6] adsorption,[7] biological treatment technology[8] and phytoremediation.[9] Advanced oxidation technologies, such as ozonation, catalytic wet oxidation, electrochemical oxidation and Fenton oxidation, can produce free radicals (such as $^{\bullet}OH$ and $^{\bullet}O_2^-$) and they have usually been used for antibiotic wastewater treatment.[10] Among them, Fenton oxidation has attracted wide attention for its strong oxidation ability and simple operation.[11] However, there are still inherent drawbacks with Fenton technology, such as the generation of iron-containing sludge, a narrow range of working pH (2–3.5), great difficulty in catalyst regeneration, and excessive consumption of H_2O_2.[12] In order to overcome these drawbacks, heterogeneous Fenton technology was developed, an iron-based solid was used to replace soluble iron ions, and the cycling of Fe^{2+}/Fe^{3+} could ensure the successive reduction of Fe^{3+} to Fe^{2+}.[13]

For iron-based heterogeneous Fenton technology, $^{\bullet}OH$ was generated mainly *via* the Hubble–Weiss cycle (eqn (1) and (2)), where Fe^{3+} reduction to Fe^{2+} (eqn (2)) was regarded as the rate-

[a]*Department of Environmental Engineering, Beijing Institute of Petrochemical Technology, Beijing 102617, PR China. E-mail: yulian@bipt.edu.cn; Tel: +86-10-81292291*

[b]*College of Fisheries, Southwest University, Chongqing, 402460, PR China*

[c]*Laboratory of Quality & Safety Risk Assessment for Tobacco, Ministry of Agriculture, Tobacco Research Institute of Chinese Academy of Agricultural Sciences, Qingdao, 266101, PR China*

controlling step, which significantly influenced the production of $^{\cdot}OH$,[14] and the active sites at the catalyst interface directly catalyzed the decomposition of H_2O_2 (eqn (3) and (4)).[15] Therefore, accelerating the Fe^{3+}/Fe^{2+} cycle is a crucial method to promote the production of $^{\cdot}OH$. There are three main methods for improving heterogeneous Fenton reactions: (1) incorporating Fe^{2+}:[16] Fe^{2+} has been introduced into the catalysts *via* different methods; (2) facilitating the regeneration of Fe^{2+}:[13] additional energy, materials and reagents (such as light, metals and redox mediators) were introduced to heterogeneous Fenton reactions; (3) accelerating the Hubble–Weiss cycle:[14] some catalyst modification methods (such as regulation of surface/interface and fabrication of composite materials) have been applied to promote the Hubble–Weiss cycle in heterogeneous Fenton reactions.

$$Fe^{2+} + H_2O_2 \rightarrow Fe^{3+} + {}^{\cdot}OH + OH^- \quad (1)$$

$$Fe^{3+} + H_2O_2 \rightarrow Fe^{2+} + HO_2^{\cdot} + H^+ \quad (2)$$

$$\equiv Fe^{2+} + H_2O_2 \rightarrow \equiv Fe^{3+} + {}^{\cdot}OH + OH^- \quad (3)$$

$$\equiv Fe^{3+} + H_2O_2 \rightarrow \equiv Fe^{2+} + HO_2^{\cdot} + H^+ \quad (4)$$

Fe_3O_4 nanoparticles (NPs) have been proven to be an efficient heterogeneous Fenton catalyst for a higher content of Fe^{2+} in the structure,[17] and rapid electron transfer between Fe^{2+} and Fe^{3+} can be achieved in a unique octahedral structure.[18] Fe^{2+} in an Fe_3O_4 octahedron was oxidized to Fe^{3+} by H_2O_2 to produce $^{\cdot}OH$ (eqn (1), k = 40–80 M^{-1} s^{-1}), and the structure of Fe_3O_4 remained unchanged.[18] Nevertheless, further reduction of the produced Fe^{3+} to Fe^{2+} by H_2O_2 was hindered, because the reaction rate was as low as 0.001–0.01 M^{-1} s^{-1} (eqn (2)).[19] Furthermore, the utilization efficiency for H_2O_2 was always relatively low because of Fe_3O_4 aggregation and a slow Fe^{3+}/Fe^{2+} cycle.[20] Therefore, excessive H_2O_2 (10–50 mmol L^{-1}) should be added for the complete degradation of organic pollutants (0.01–0.3 mmol L^{-1}).[20] Since Fe_3O_4 NPs inevitably generated interfacial or dissolved Fe^{3+} during the Fenton reaction, some electron donors were needed to reduce Fe^{3+} to Fe^{2+}. Furthermore, Fe_3O_4 NPs were apt to agglomerate during the Fenton reaction.[21] It was proved that loading Fe_3O_4 NPs can suppress both agglomeration and the leakage of Fe ions.[22]

Recently, it was found that loading metal oxide NPs onto MOFs could overcome the drawbacks of a single catalyst. Among iron-based MOFs, Materials of Institute Lavoisier-type frameworks (MILs) were proved to be efficient catalysts for Fenton-like reactions. MILs showed many advantages, such as high catalytic activity, adjustable size and shape, well-defined pore architecture, high specific surface area, excellent photoresponsiveness, tailorable chemical composition and high aqueous stability.[23] Fe_3O_4 NPs were loaded onto MILs to construct composites, and the individual drawbacks could be improved.[16] The combination of Fe_3O_4 NPs and MIL-100(Fe) was a feasible strategy. The composite showed excellent catalytic activity and possessed the advantages of MIL-100(Fe) and Fe_3O_4 NPs.[16] Liang *et al.*[24] synthesized magnetic MIL-100(Fe). The catalyst showed excellent performance for the degradation of oxytetracycline hydrochloride *via* photo-Fenton under visible sunlight. They also constructed a CuS/Fe_3O_4@MIL-100(Fe)/vis/H_2O_2 system, using which, 95.31% of oxytetracycline hydrochloride could be removed.[25] Gong *et al.*[26] prepared Fe_3O_4@GO@MIL-100(Fe), and nearly 100% of 2,4-dichlorophenol could be removed by Fe_3O_4@GO@MIL-100(Fe) in a photo-Fenton reaction.

Although the Fe_3O_4/MIL-100(Fe) composite showed excellent catalytic activity for a heterogeneous Fenton reaction, the low Fe^{2+}/Fe^{3+} cycle rate limited its extensive application in Fenton processes.[27] Recently, heterogeneous Fenton catalysts were loaded onto various organic or inorganic materials, such as organic membranes, resins, zeolite, silicon, clay, activated carbon and graphene oxide (GO).[23] Catalysts interacting with supports may produce new active sites; the supports could also act as an electron bridge; the electrons could transfer between pollutants; and H_2O_2 and Fe species promote Fe^{3+} reduction to Fe^{2+}.[28] GO is a good conductive material, and Fe_3O_4 NPs loaded onto GO were used to overcome the limitations mentioned.[13,29] It acted as a "bridge", when electrons from organic oxidation were transferred to the $\equiv Fe^{3+}$ close to GO. Agglomeration of Fe_3O_4 NPs was hindered by loading Fe_3O_4 NPs onto GO sheets,[30] and its rich oxygen-containing functional groups were favorable for pollutant adsorption, thus realizing effective degradation of pollutants.[31] It is expected that loading of Fe_3O_4/MIL-100(Fe) composite onto GO could produce marked changes to its structure, performance and activity in a heterogeneous Fenton reaction.

Enlightened by the above analysis, we synthesized a GO/MIL-100(Fe)@Fe_3O_4 heterostructure using Fe_3O_4 NPs as the active component and GO as an electron bridge to MIL-100(Fe) for the photo-Fenton degradation of ERY. The surface morphology, crystalline structure, elemental composition and optical adsorption properties of the catalyst were characterized. The catalytic performance, the influences of operating parameters (such as pH conditions, H_2O_2 concentration and catalyst dosage) on ERY removal, and the stability of the catalyst, were systematically evaluated. GO/MIL-100(Fe)@Fe_3O_4 showed enhanced photo-Fenton catalytic activity for ERY degradation compared to Fe_3O_4 NPs, MIL-100(Fe) or MIL-100(Fe)@Fe_3O_4, which can be ascribed to the synergistic effects between Fe_3O_4 NPs, MIL-100(Fe) and GO. In a GO/MIL-100(Fe)@Fe_3O_4 + H_2O_2 + vis system, the electrons from organics and MIL-100(Fe) can be effectively transferred to Fe_3O_4 NPs by GO, thus accelerating the Fe^{3+}/Fe^{2+} cycle, and enhancing the catalytic activity.

2. Experimental

2.1. Materials

All the solvents and regents were of at least analytical grade and used without purification. $FeCl_2 \cdot 4H_2O$ (99%), $FeCl_3 \cdot 6H_2O$ (99%), NaOH (98%), HCl (36–38%), hydrogen peroxide (H_2O_2, 30%), silver nitrate ($AgNO_3$, 99.8%), 1,3,5-benzenetricarboxylic acid (H_3BTC, 98%), ammonium oxalate (AO, 99%), *tert*-butyl alcohol (TBA, 99.8%), *p*-benzoquinone (BQ, 99.5%), $NaHCO_3$ (99%), NaH_2PO_4 (99%), NaCl (99%), Na_2SO_4 (99%), $NaNO_3$

(99%) and humic acid (HA, 99%) were obtained from Sinopharm Chemical Reagent Co., Ltd. Erythromycin (ERY, 85%) was obtained from Aladdin Reagent (Shanghai) Co., Ltd. All solutions were prepared using deionized Milli-Q water (18.2 MΩ).

2.2. Preparation of samples

2.2.1. Synthesis of Fe_3O_4 NPs. Fe_3O_4 NPs were prepared by a chemical coprecipitation method.[32] Briefly, $FeCl_2 \cdot 4H_2O$ (2.0 g, 10.1 mmol) and $FeCl_3 \cdot 6H_2O$ (5.2 g, 19.2 mmol) were dissolved in deionized water (25 mL), followed by the addition of 0.85 mL of concentrated hydrochloric acid. The obtained solution was added into a three-necked round flask (500 mL), then 100 mL of NaOH solution (1.2 mol L^{-1}) was added dropwise into the above solution under non-magnetic agitation and an N_2 atmosphere at 80 °C. Afterwards, the obtained suspension was aged for 30 min and cooled to room temperature. Finally, the black precipitate was separated from the suspension by magnetic separation and rinsed with deionized water several times until the pH of the scrubbing solution achieved a neutral value, and then dried through freeze drying for 24 h.

2.2.2. Synthesis of partially reduced GO. Partially reduced GO was prepared *via* a one-step hydrothermal method.[28] In a typical process, 20 mg of GO powder and 0.08 g of ascorbic acid were added to 10 mL of deionized water. Then, the mixture was treated under ultrasonication for 30 min, transferred to a Teflon-lined autoclave (100 mL), and kept at 180 °C for 16 h. After cooling to 25 °C, a hydrogel was obtained, which was dipped in ethanol solution (15%) for 24 h to remove the remaining precursor. Finally, the sample was treated by freeze drying for 24 h to produce partially reduced GO.

2.2.3. Synthesis of MIL-100(Fe). MIL-100(Fe) was prepared by a hydrothermal method.[33] $FeCl_3 \cdot 6H_2O$ (960.1 mg, 3.55 mmol) and benzene-1,3,5-tricarboxylic acid (H_3BTC, 501.5 mg, 2.39 mmol) were dissolved in deionized water (20 mL). The mixture was stirred for 30 min, then added to a Teflon sealed-autoclave, and heated at 150 °C for 24 h.[33] The obtained red-brown samples were centrifuged, rinsed with deionized water, and dried through freeze drying for 24 h.

2.2.4. Synthesis of GO/MIL-100(Fe). GO/MIL-100(Fe) was prepared by a hydrothermal method.[33] A suspension of H_3BTC (501.5 mg, 2.39 mmol) and obtained GO (15 mg) in deionized water (50 mL) was prepared by stirring for 1 h. Then, $FeCl_3 \cdot 6H_2O$ (960.1 mg, 3.55 mmol) was dissolved in the above H_3BTC–GO suspension. The mixture was stirred for 30 min, then added to a Teflon sealed autoclave, and heated at 150 °C for 24 h. The obtained samples were centrifuged, rinsed with deionized water, and dried through freeze drying for 24 h.

2.2.5. Synthesis of GO/MIL-100(Fe)@Fe_3O_4. $FeCl_2 \cdot 4H_2O$ (2.0 g, 10.1 mmol) and $FeCl_3 \cdot 6H_2O$ (5.2 g, 19.2 mmol) were dissolved in deionized water (50 mL), followed by the addition of 0.85 mL of concentrated hydrochloric acid and 0.48 g of obtained GO/MIL-100(Fe), then stirred for 30 min. The obtained suspension was added into a three-necked round flask (500 mL), then 100 mL of NaOH solution (1.2 mol L^{-1}) was added dropwise into the above suspension under non-magnetic agitation and an N_2 atmosphere at 80 °C. Then, the obtained GO/MIL-100(Fe)@Fe_3O_4 suspension was aged for 30 min and cooled to room temperature. Finally, the black precipitate was separated from the suspension by magnetic separation and rinsed with deionized water several times, and dried through freeze drying for 24 h.

2.3. Characterization

The sizes and microstructures of the materials were examined using transmission electron microscopy (TEM, JSM-2200FS, JEOL, Japan) with 200 kV accelerating voltage. The X-ray powder diffraction (XRD) patterns were obtained using an X-ray diffractometer (D8 Focus, Brooke, Germany), where the detection conditions were 40 kV, 40 mA, and a 2θ range of 5°–80°. Raman spectra were obtained by a confocal Raman spectroscopic system (inVia Qontor, Renishaw, UK) using a 532 nm excitation laser. Information on the surface chemical state of the materials was obtained using X-ray photoelectron spectroscopy (XPS, PHI5300, PerkinElmer, USA). The surface areas and pore structures were analyzed by N_2 adsorption–desorption on an ASAP 2020HD88 (Micromeritics, America) using the BET and BJH methods. The UV-vis diffuse reflectance spectra (UV-vis DRS) were obtained with a Specord 210 Plus UV-visible spectrophotometer (Jena, Germany). Photoluminescence (PL) spectra were obtained *via* a steady-state/transient fluorescence spectrometer (Edinburgh FLS1000, United Kingdom).

2.4. Experimental procedures

The experiments were conducted in a photochemical reaction system (BL-GHX-CH500, Xi'an Depai Biotech. Co., Ltd, China). A 300 W xenon lamp (PLS-SXE300/300UV, Perfect Light, China) with a cutoff filter (420 nm) was applied as a visible light source, and the light source was 15 cm above the surface of the solution. The solution pH, H_2O_2 concentration and catalyst dosage were optimized. A determined amount of catalyst was added uniformly to 100 mL of ERY solution of a certain concentration, and the pH of solution was adjusted by adding 0.1 mol L^{-1} HNO_3 or 0.1 mol L^{-1} NaOH. The suspension was stirred in the dark for 30 min until adsorption equilibrium, then the xenon lamp was switched on and a determined amount of H_2O_2 was added to the suspension to start the reaction. Suspension samples were taken at given time intervals using a 4.0 mL syringe, and immediately filtered with 0.22 μm drainage syringe filters (Tianjin Branch Billion Lung, China), and a quenching agent (1.0 mL) was rapidly added to the filtrate to quench reactive species. The filtrate was diluted 10 fold and tested with a UV-vis detector (Agilent Cary 300 UV-vis Spectrophotometer, USA) at 583 nm in methyl violet solution. Erythromycin reacted with methyl violet to form a coordination compound, and the concentration of erythromycin was calculated based on the concentration of the coordination compound. The removal efficiency of ERY was calculated as: $(C_0 - C_t)/C_0 \times 100\%$, where C_0 is the initial concentration of ERY, and C_t is the concentration at time t. The used catalysts were recovered by filtration, and washed with alcohol and deionized water, dried under vacuum, then reused for the next cycle, to evaluate their

reusability. The concentrations of iron ions leaching from the catalysts were measured by ICP-MS (Thermo Fisher iCAP Q, America). To confirm the primary active species in the degradation reaction, scavengers like 20 mmol L^{-1} tertiary butanol (TBA), silver nitrate ($AgNO_3$), ammonium oxalate (AO), and *p*-benzoquinone (BQ) were added to the solution before adding H_2O_2. The active species can be confirmed by the effect of different scavengers on ERY removal.

3. Results and discussion

3.1. Characterization of catalysts

The surface morphology and structural characteristics of GO/MIL-100(Fe)@Fe_3O_4 were investigated by TEM. As can be seen in Fig. 1a, GO showed a silk-like wrinkled structure, and more active nanoparticles can be anchored onto wrinkled GO. Fe_3O_4 NPs showed a spherical morphology with a rough surface, and the average diameter was about 12 nm (Fig. 1b). MIL-100(Fe) with a side length of about 40 nm displayed irregular shapes (Fig. 1c). For GO/MIL-100(Fe)@Fe_3O_4 (Fig. 1d), MIL-100(Fe) and Fe_3O_4 NPs were uniformly anchored onto the GO surface, suggesting the successful loading of MIL-100(Fe) and Fe_3O_4 NPs onto the GO surface.

The crystal structures of the catalysts were analyzed by their XRD patterns (Fig. 2). For GO, the peak at $2\theta = 10.4°$ corresponded to the (001) crystal plane. After reduction, the peak at $2\theta = 10.4°$ disappeared, and a broad reflection peak appeared at $2\theta = 25.46°$, which can be ascribed to the (002) crystal plane of reduced GO.[34] For Fe_3O_4 NPs, the peaks at $2\theta =$ 18.51° (111), 30.26° (220), 35.61° (311), 43.26° (400), 54.30° (422), 57.19° (511), and 62.97° (440) corresponded to cubic

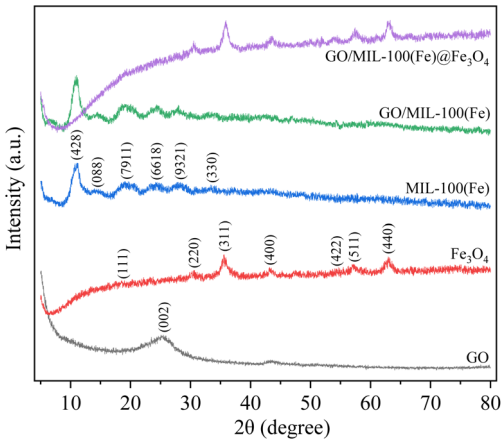

Fig. 2 XRD patterns of GO, Fe_3O_4 NPs, MIL-100(Fe), GO/MIL-100(Fe) and GO/MIL-100(Fe)@Fe_3O_4.

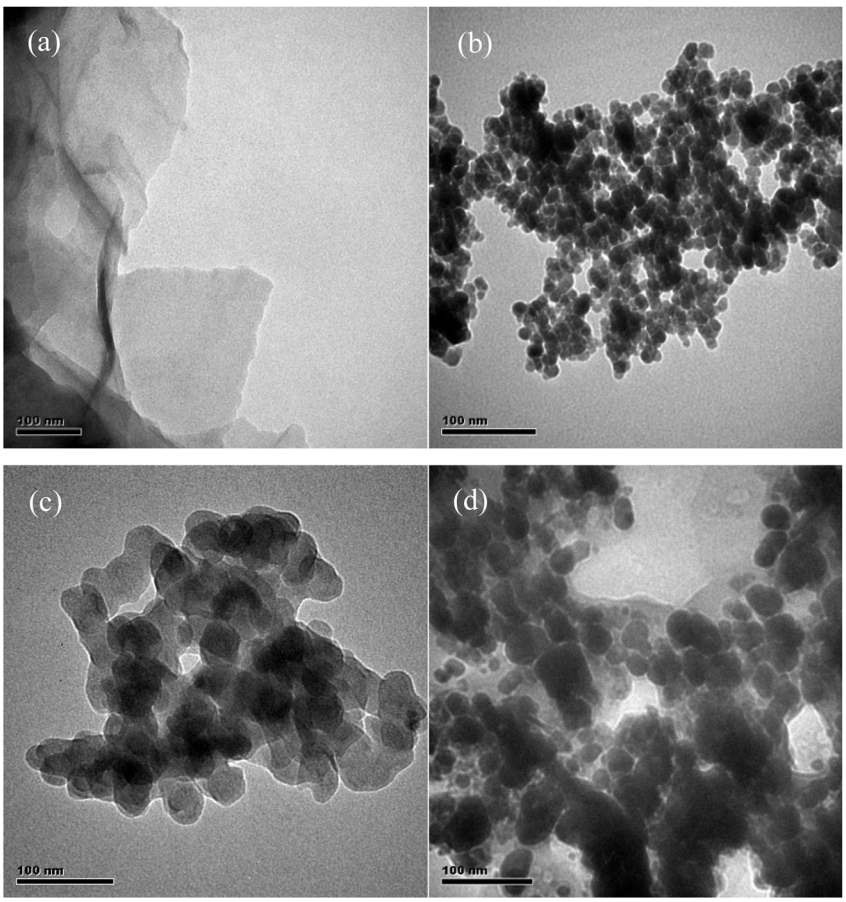

Fig. 1 TEM images of GO (a), Fe_3O_4 NPs (b), MIL-100(Fe) (c) and GO/MIL-100(Fe)@Fe_3O_4 (d).

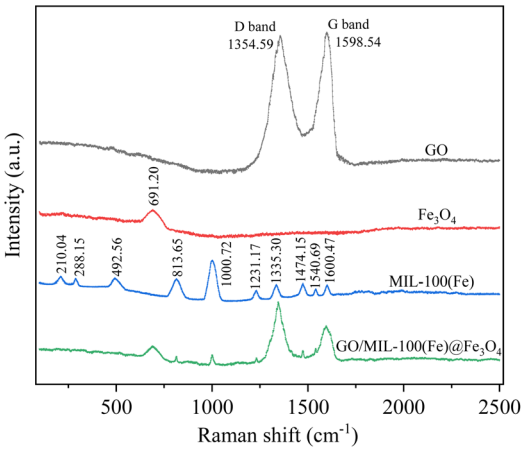

Fig. 3 Raman spectra of GO, Fe_3O_4 NPs, MIL-100(Fe) and GO/MIL-100(Fe)@Fe_3O_4.

Fe_3O_4 with the inverse spinel structure [JCPDS card no. 19-0629],[35] indicating the successful synthesis of Fe_3O_4 NPs. The main characteristic peaks for MIL-100(Fe) were in accordance with the simulated ones from crystal data.[33] The diffraction peaks at 2θ = 11.16° (428), 13.96° (088), 19.09° (7911), 24.16° (6618), 27.93° (9321), and 33.39° (330) were also coincident with those reported for MIL-100(Fe). In the XRD pattern of GO/MIL-100(Fe)@Fe_3O_4, the diffraction peaks for cubic Fe_3O_4 and MIL-100(Fe) can be found. However, in neither the XRD pattern of GO/MIL-100(Fe) nor that for GO/MIL-100(Fe)@Fe_3O_4, did any distinct peaks of GO appear, which may be ascribed to the small size of GO crystallites. These results suggested the successful synthesis of GO/MIL-100(Fe)@Fe_3O_4.

To further confirm the existence of GO in GO/MIL-100(Fe)@Fe_3O_4, the Raman spectra of GO, Fe_3O_4 NPs, MIL-100(Fe) and GO/MIL-100(Fe)@Fe_3O_4 were measured (Fig. 3). The GO spectrum showed two broad peaks at 1354.59 and 1598.54 cm^{-1}, which were ascribed to the specific D (1354.59 cm^{-1}) and G (1598.54 cm^{-1}) bands corresponding to the vibration of sp^3 carbons appearing in the disordered region (or defects) in the graphite lattice and the C=C stretching of sp^2-hybridized carbon atoms, respectively.[26] Fe_3O_4 NPs showed a rather simple spectrum, where only one A_{1g} vibration peak could be observed at 691.20 cm^{-1}.[36] Several peaks could be found in the spectrum of MIL-100(Fe). The peaks at 210.04 cm^{-1}, 288.15 cm^{-1}, 492.56 cm^{-1}, 1474.15 cm^{-1} and 1540.69 cm^{-1} were characteristic of vibrational modes, which were directly related to Fe^{3+} and Fe^{2+} in MIL-100(Fe).[37] The peak at 813.65 cm^{-1} can be ascribed to –COO– functional group bonding to the benzene ring, while H_3BTC in-plane vibrations were confirmed by the peaks at 1000.72 cm^{-1}, 1231.17 cm^{-1}, 1335.30 cm^{-1} and 1600.47 cm^{-1}.[37] The main peaks for GO, Fe_3O_4 NPs and MIL-100(Fe) can be found in the spectra of GO/MIL-100(Fe)@Fe_3O_4. The Raman spectrum of GO/MIL-100(Fe)@Fe_3O_4 also contained D and G bands, confirming the presence of GO and Fe_3O_4 NPs in the composite.[37] However, partial Raman peaks for MIL-100(Fe) tended to be weak and even disappeared after the introduction of Fe_3O_4 NPs and GO, which can be ascribed to the sheltering of MIL-100(Fe) by GO and Fe_3O_4 NPs. The peak at 1474.15 cm^{-1} changed, which was related to the change in organic ligand coordination with Fe^{3+} and Fe^{2+}, because carboxylate vibrations actually appeared in this region.[38] The above results confirmed that GO and Fe_3O_4 NPs introduced some distortion into the MIL-100(Fe) structure.[38]

The surface element content and valence states of GO/MIL-100(Fe)@Fe_3O_4 were tested by XPS. Fig. 4a shows the XPS full spectrum, clearly indicating the presence of C, O and Fe in GO/MIL-100(Fe)@Fe_3O_4 and MIL-100(Fe)@Fe_3O_4. The C 1s spectrum in Fig. 4b could be divided into three peaks: 284.63 eV, 285.63 eV and 288.78 eV, corresponding to the characteristic peaks of C–C, C–O–C, and O–C=O.[39] The peaks located at binding energies of 284.63 eV and 288.78 eV were related to the benzene ring and carboxylic functional groups in MIL-100(Fe).[16] For the spectrum of GO/MIL-100(Fe)@Fe_3O_4, the peak at 285.63 eV was derived from C–O in GO,[27] which cannot be found in MIL-100(Fe)@Fe_3O_4. Additionally, the strength of the peaks at 284.63 eV and 288.78 eV increased in GO/MIL-100(Fe)@Fe_3O_4 compared with those of MIL-100(Fe)@Fe_3O_4, suggesting that GO promoted the generation of MIL-100(Fe). The O 1s spectrum can be divided into two peaks at 530.78 eV and 532.83 eV, which can be ascribed to the oxygen element of organic linkers in MIL-100(Fe) and Fe–O bonds respectively.[16] As for GO/MIL-100(Fe)@Fe_3O_4, the peaks at 530.78 eV and 532.83 eV shifted to higher binding energy (530.78 eV and 532.76 eV for MIL-100(Fe)@Fe_3O_4), which can be ascribed to the C–O functional groups from GO.[26] As can be seen from Fig. 4d, the Fe 2p fitted peaks of GO/MIL-100(Fe)@Fe_3O_4 showed two obvious peaks at 711.58 eV and 725.43 eV (712.48 eV and 725.88 eV for MIL-100(Fe)@Fe_3O_4), which were attributed to Fe $2p_{3/2}$ and Fe $2p_{1/2}$ peaks for Fe species. For GO/MIL-100(Fe)@Fe_3O_4, the Fe 2p spectra can be divided into four peaks at 711.22 eV, 713.24 eV, 724.57 eV and 726.00 eV, and two peaks at 711.22 eV and 724.57 eV, respectively, corresponding to Fe $2p_{3/2}$ and Fe $2p_{1/2}$ for Fe^{2+}, while two peaks at 713.24 eV and 726.00 eV can be ascribed to Fe $2p_{3/2}$ and Fe $2p_{1/2}$ for Fe^{3+}, further indicating that Fe species existed as a mixed-valence state (Fe^{2+} and Fe^{3+}).[39] The ratio of Fe^{2+}/Fe^{3+} can be calculated according to the peak area of Fe $2p_{3/2}$, as can be seen from Fig. 4d, after the introduction of GO, the peak area of Fe $2p_{3/2}$ for Fe^{2+} increased, which indicated that GO was favorable for the formation of Fe^{2+} in GO/MIL-100(Fe)@Fe_3O_4. The above analysis indicated that GO/MIL-100(Fe)@Fe_3O_4 had been successfully synthesized.

N_2 adsorption–desorption isotherms were used to analyze the surface area and pore structure of Fe_3O_4 NPs, MIL-100(Fe)@Fe_3O_4 and GO/MIL-100(Fe)@Fe_3O_4. As shown in Fig. 5, Fe_3O_4 NPs showed a type IV isotherm with hysteresis (P/P_0 = 0.5–0.9), according to the Brunauer–Deming–Deming–Teller (BDDT) classification,[28] which characterize a mesoporous structure. The adsorption and desorption isotherms remained almost horizontal and parallel, indicating a IUPAC type H_4 hysteresis loop. The type IV isotherm with a type H_4 hysteresis loop indicated the existence of narrow lamellar slit-like pores. After loading Fe_3O_4 NPs onto MIL-100(Fe), MIL-100(Fe)@Fe_3O_4 showed a type IV isotherm with a type H_3 hysteresis loop, suggesting a mesoporous structure on the outer layer of the catalyst.[16] GO/MIL-

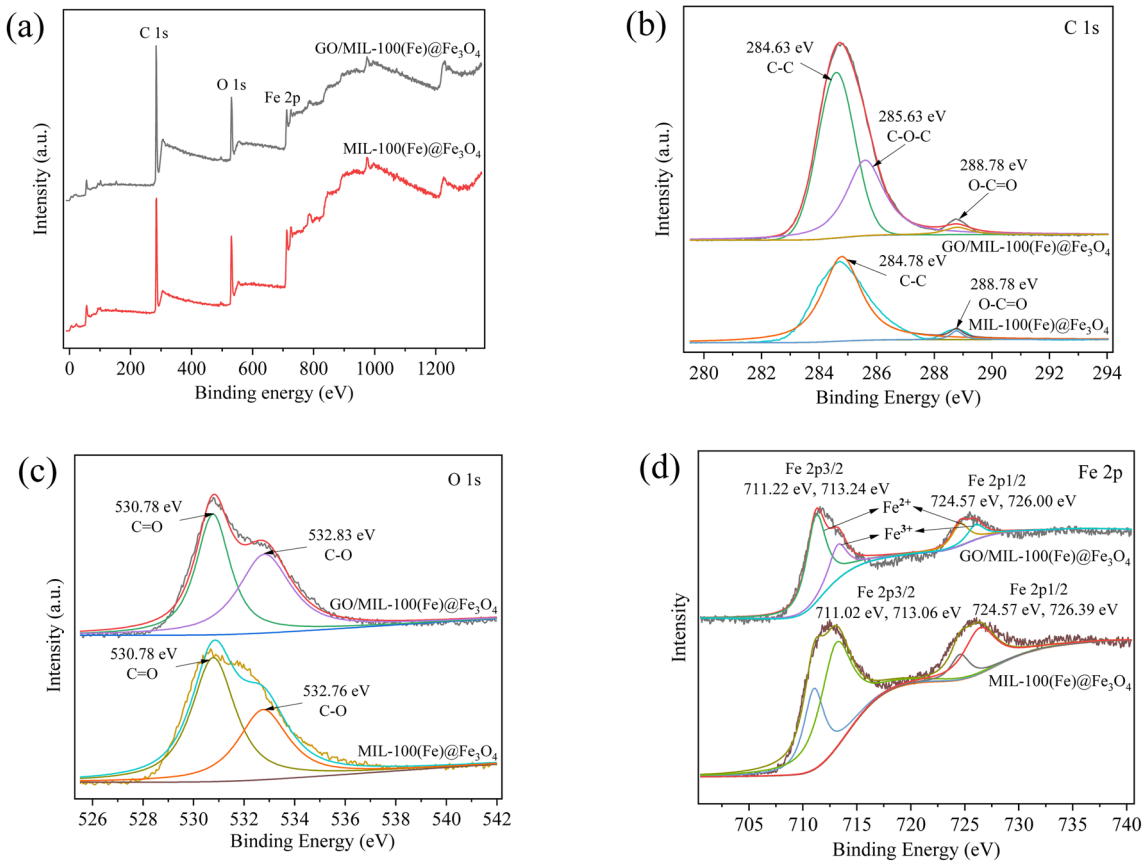

Fig. 4 XPS analysis of the catalysts: full-scan spectrum (a), C 1s (b), O 1s (c) and Fe 2p (d).

100(Fe)@Fe_3O_4 showed the same type of isotherm and hysteresis as MIL-100(Fe)@Fe_3O_4, but the hysteresis loop was larger, suggesting an increase in pore diameter.

The specific surface areas of Fe_3O_4 NPs, MIL-100(Fe)@Fe_3O_4 and GO/MIL-100(Fe)@Fe_3O_4 by BET measurement, were 54.25 $m^2\ g^{-1}$, 684.53 $m^2\ g^{-1}$ and 841.46 $m^2\ g^{-1}$, respectively, suggesting that MIL-100(Fe) and GO can significantly increase the specific surface area of the catalyst. Additionally, the pore size distribution centers for GO/MIL-100(Fe)@Fe_3O_4 were around 3.98 nm and 19.35 nm, which were larger than those of Fe_3O_4 NPs or MIL-100(Fe)@Fe_3O_4. These properties promoted the adequate contact of GO/MIL-100(Fe)@Fe_3O_4 with pollutants. The high surface area and porosity of GO/MIL-100(Fe)@Fe_3O_4 would promote the adsorption and diffusion of pollutants to the active sites during degradation, endowing the catalyst with high catalytic activity.

UV-vis DRS spectroscopy was used to analyze the optical response of the catalyst. As can be seen in Fig. 6a, MIL-100(Fe) showed wide and intense absorption capacity for UV and visible light in the range 250–600 nm. The absorption of ultraviolet

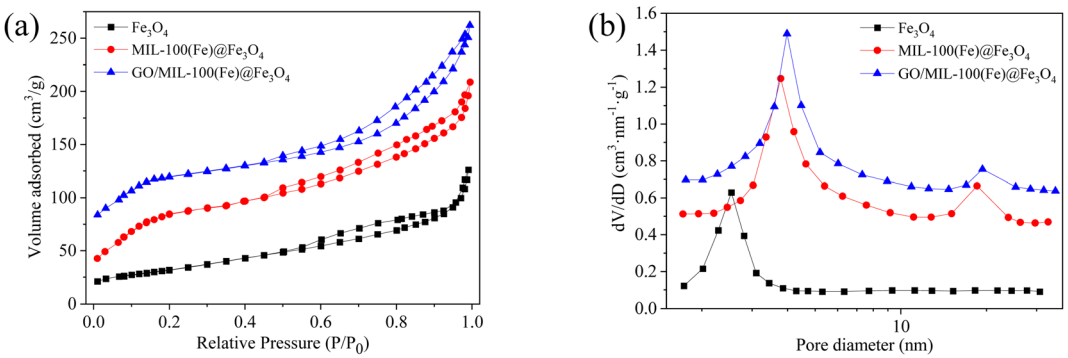

Fig. 5 N_2 adsorption–desorption isotherms of Fe_3O_4 NPs, MIL-100(Fe)@Fe_3O_4 and GO/MIL-100(Fe)@Fe_3O_4 (a), and the corresponding BJH pore size distributions (b).

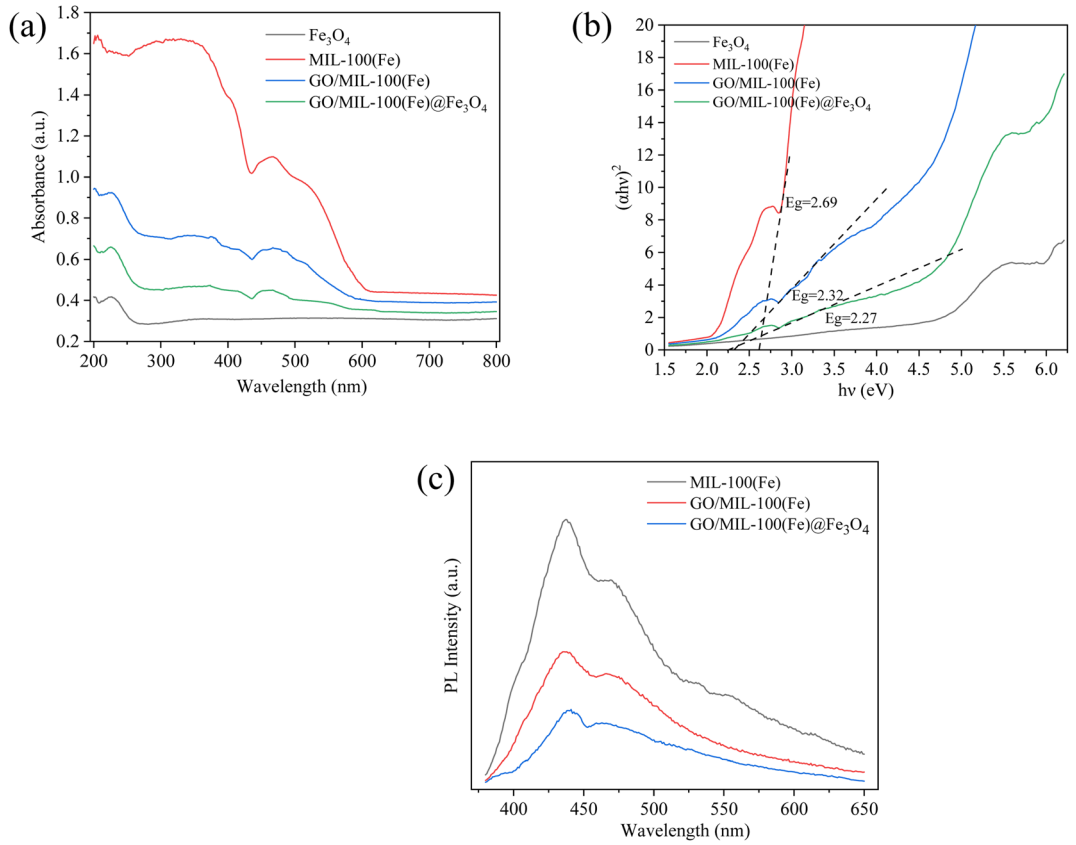

Fig. 6 UV-vis diffuse reflection spectra of catalysts (a), the corresponding plots of $(\alpha h\nu)^2$ *vs.* photon energy ($h\nu$) (b), and photoluminescence (PL) spectra (c).

light can be ascribed to ligand-to-metal charge transfer,[40] while the strong ability to absorb visible light was attributed to the Fe_3-μ_3-oxo cluster in MIL-100(Fe).[16] After the introduction of Fe_3O_4 NPs and GO, the composite showed a similar absorption edge to MIL-100(Fe) in the range 250–600 nm, indicating that the inherent band gap of GO/MIL-100(Fe)@Fe_3O_4 was derived mainly from electron transfer from the valence band (VB) to the conduction band (CB) of MIL-100(Fe).[16] This suggested that GO/MIL-100(Fe)@Fe_3O_4 may commendably utilize incident light to generate more active species.[16] Meanwhile, the band gap energies can be calculated with Tauc plots ($(\alpha h\nu)^n = A(h\nu - E_g)$), where α, h, ν, A and E_g are the absorption coefficient, Planck constant, light frequency, proportionality constant and band gap, respectively (for a direct band gap semiconductor, $n = 2$).[16] The calculated band-gap values were 2.69 eV, 2.32 eV and 2.27 eV for MIL-100(Fe), GO/MIL-100(Fe) and GO/MIL-100(Fe)@Fe_3O_4, respectively (Fig. 6b). With improved absorption of visible light, GO/MIL-100(Fe)@Fe_3O_4 may produce more electrons to reduce Fe^{3+} to Fe^{2+} and generate more reactive oxidation species under light radiation.

Charge transfer influenced the photocatalytic reaction. The influence of GO and Fe_3O_4 in GO/MIL-100(Fe)@Fe_3O_4 on the separation of photogenerated electrons and holes can be clarified using photoluminescence emission spectra. Basically, lower PL emission peaks suggested more efficient separation of photogenerated electrons and holes.[16] As shown in Fig. 6c, a broad PL peak can be seen at around 437 nm, and this could be due to the recombination of self-trapped excitation. The intensity of PL emission peaks decreased in sequence: MIL-100(Fe) > GO/MIL-100(Fe) > GO/MIL-100(Fe)@Fe_3O_4, suggesting that GO/MIL-100(Fe)@Fe_3O_4 may show the best photo-Fenton activity, revealing that the recombination of photogenerated electron–hole pairs can be largely inhibited by the introduction of GO and Fe_3O_4 into GO/MIL-100(Fe)@Fe_3O_4.

3.2. Catalytic performance

The catalytic performance of GO/MIL-100(Fe)@Fe_3O_4 was evaluated by ERY removal. As can be seen from Fig. 7a, in the absence of catalysts, the concentration of ERY remained almost unchanged under visible-light irradiation. 41.7% of ERY in the Fe_3O_4 + H_2O_2 + vis system was removed within 60 min. The removal efficiency for ERY in the GO@Fe_3O_4 + H_2O_2 + vis system increased to 68.7%, indicating that GO played an important role in the photo-Fenton reaction. Additionally, in the MIL-100(Fe) + H_2O_2 + vis and MIL-100(Fe)@Fe_3O_4 + H_2O_2 + vis systems, ERY removal efficiencies were 74.4% and 86.8%, respectively, suggesting that the catalytic activity of MIL-100(Fe)@Fe_3O_4, combining Fe_3O_4 NPs with MIL-100(Fe), needed to be improved. Nevertheless, under the same experimental conditions, 97.3% of ERY was removed in the GO/MIL-100(Fe)@Fe_3O_4 + H_2O_2 + vis system, achieving the maximum value. In the GO/MIL-100(Fe)

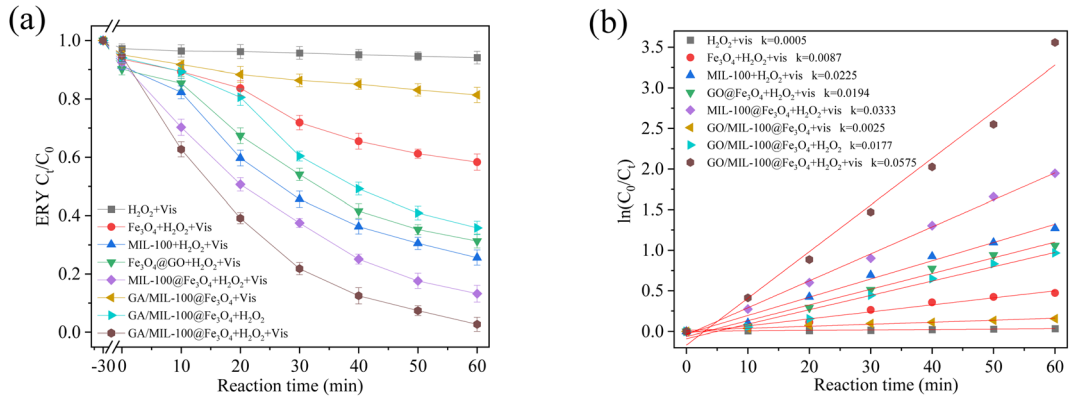

Fig. 7 Degradation curves in different reaction systems (a), and the corresponding degradation kinetics of the degradation curves (pseudo-first-order kinetics model) (b). pH = 4.03, $[H_2O_2]_0$ = 10 mmol L^{-1}, $[catalyst]_0$ = 0.1 g L^{-1}, $[ERY]_0$ = 0.1 mmol L^{-1}, T = 30 °C.

@Fe_3O_4/dark system, only a Fenton-like reaction took place for the degradation of ERY. Therefore, the increased removal of ERY in the GO/MIL-100(Fe)@Fe_3O_4/vis system was ascribed to the photo-Fenton-like reaction. Thus H_2O_2 and visible-light irradiation were sufficient, and more $^{\cdot}OH$ and $HO_2^{\cdot}$ were generated for ERY degradation.

The kinetics of the reactions were analyzed and the reaction processes followed the pseudo-first-order kinetic equation ($K_{app}t = -\ln(C/C_0)$), where K_{app} is the first-order kinetic constant (min^{-1}), t is the reaction time (min), C_0 is the original concentration of ERY solution (mmol L^{-1}), and C is the concentration of ERY solution after reaction for a period (mmol L^{-1}). As shown in Fig. 7b, under dark conditions, the apparent rate constant of the GO/MIL-100(Fe)@Fe_3O_4 + H_2O_2 system was 0.0177 min^{-1}. After introducing light, the apparent rate constant increased to 0.0575 min^{-1}. This suggested that visible light can promote the decomposition of H_2O_2 into more $^{\cdot}OH$, thus enhancing removal efficiency for ERY. The apparent rate constant of the GO/MIL-100(Fe)@Fe_3O_4 + H_2O_2 + vis system was 2.96 times that of the GO@Fe_3O_4 + H_2O_2 + vis system and 2.56 times that of the MIL-100(Fe) + H_2O_2 + vis system, suggesting a probable synergistic effect among Fe_3O_4, GO and MIL-100(Fe). The synergistic effect was evaluated by calculating the synergistic factor ($F > 1$) ($F = K_{GO/MIL\text{-}100(Fe)@Fe_3O_4}/(K_{Fe_3O_4@GO} + K_{MIL\text{-}100(Fe)})$), where $K_{GO/MIL\text{-}100(Fe)@Fe3O_4}$, $K_{Fe_3O_4@GO}$ and $K_{MIL\text{-}100(Fe)}$ are the apparent rate constants of GO/MIL-100(Fe)@Fe_3O_4, GO@Fe_3O_4 and MIL-100(Fe), respectively.[39] After calculation, F = 1.37, confirming the synergistic effect among Fe_3O_4, GO and MIL-100(Fe). The enhanced ERY removal efficiency in the GO/MIL-100(Fe)@Fe_3O_4 + H_2O_2 + vis system can be ascribed to: (1) light-induced H_2O_2 generated more $^{\cdot}OH$ (eqn (5)) and accelerated the Fe^{2+}/Fe^{3+} cycle (eqn (1), (2) and (6)); (2) GO as an electron transfer channel immediately transferred electrons from the conduction band of MIL-100(Fe) to the surface of the Fe_3O_4 NPs, hindering recombination of e^-–h^+ pairs; (3) GO combined with Fe_3O_4 NPs and MIL-100(Fe) greatly promoted the contact of ERY and active sites in the composite.

$$H_2O_2 + h\nu \rightarrow 2^{\cdot}OH \quad (5)$$

$$Fe^{3+} + HO_2^{\cdot} \rightarrow Fe^{2+} + O_2 + H^+ \quad (6)$$

3.3. Effects of solution pH, H_2O_2 concentration and catalyst dosage

The initial solution pH directly influenced active species generation, and it was an important influencing factor for ERY degradation. When the initial solution pH increased from 3.02 to 4.03, the ERY degradation efficiency increased from 93.8% to 97.3% (Fig. 8a), and the apparent rate constant increased from 0.0446 min^{-1} to 0.0575 min^{-1} (Fig. 8b). This was because acidic conditions were favorable for the reaction between Fe^{2+} and H_2O_2 to produce $^{\cdot}OH$. However, under acidic conditions, $^{\cdot}O_2^-$ was consumed and inhibited, so too low a pH may decrease ERY removal efficiency and reaction rate. When the pH further increased from 4.03 to 8.98, the degradation efficiency decreased from 97.3% to 52.2%. The decreased degradation efficiency can be ascribed to: (1) increased pH may lead to aggregation of Fe_3O_4 NPs; (2) alkaline conditions may lead to the direct decomposition of H_2O_2 into inactive species; (3) increased pH results in negative charge over the catalyst surface and ERY deprotonation, causing mutual repulsion between ERY and the catalyst.[39] Overall, ERY degradation efficiencies were above 50% in the pH range of 3.02–8.98, indicating the excellent catalytic activity of the catalyst under a wide pH range.

H_2O_2 concentration also greatly influenced the photo-Fenton reaction, because it greatly influenced the generation and amount of active species. As shown in Fig. 9a, when the concentration of H_2O_2 increased from 5.0 mmol L^{-1} to 20.0 mmol L^{-1}, the removal efficiency increased from 74.4% to 97.9% (within 60 min of reaction), and the related reaction rate constant increased from 0.0216 min^{-1} to 0.0622 min^{-1}. The degradation efficiency and related rate constant achieved their maximum values when the concentration of H_2O_2 was 20.0 mmol L^{-1}, because the increased H_2O_2 concentration promoted more production of $^{\cdot}OH$. But as the concentration of H_2O_2 further increased to 50.0 mmol L^{-1}, ERY removal efficiency decreased gradually. The probable reasons for these results were: (1) limited surface active sites on the catalyst limited the degradation efficiency; (2) excessive H_2O_2 would capture $^{\cdot}OH$ and quench $^{\cdot}OH$ (eqn (7)); (3) $^{\cdot}OOH$ competing with $^{\cdot}OH$ leads to the useless consumption of reactive species (eqn (8)).

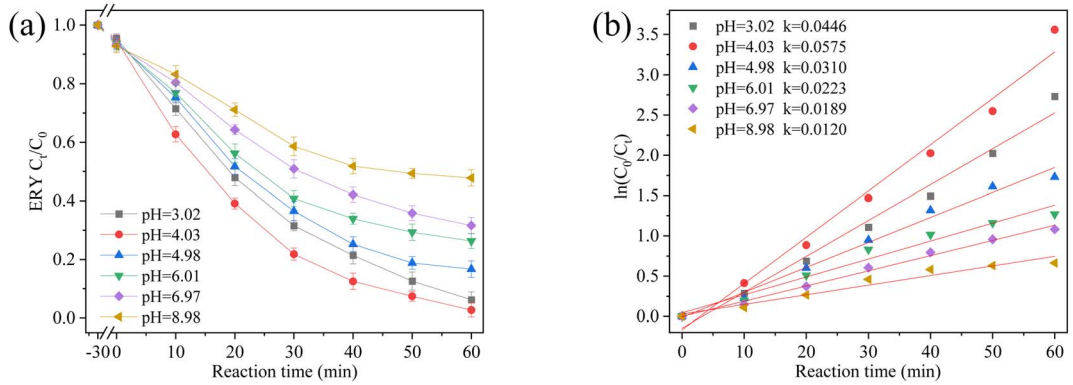

Fig. 8 The effect of the initial pH on the photo-Fenton degradation of ERY (a), and kinetic analysis of the degradation of ERY at different initial pH levels (pseudo-first-order kinetics model) (b). $[H_2O_2]_0 = 10$ mmol L^{-1}, $[catalyst]_0 = 0.1$ g L^{-1}, $[ERY]_0 = 0.1$ mmol L^{-1}, $T = 30$ °C.

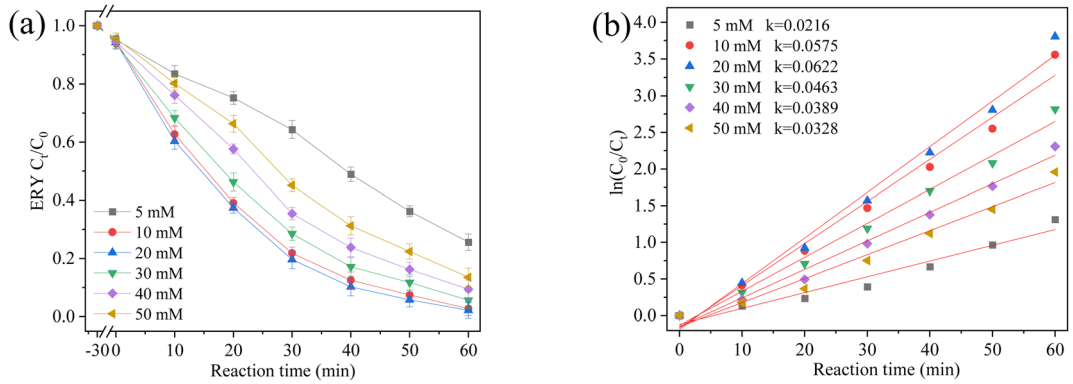

Fig. 9 Effect of the initial H_2O_2 concentration on the photo-Fenton degradation of ERY (a), and kinetic analysis of the degradation of ERY at different initial H_2O_2 concentrations (pseudo-first-order kinetics model) (b). pH = 4.03, $[catalyst]_0 = 0.1$ g L^{-1}, $[ERY]_0 = 0.1$ mmol L^{-1}, $T = 30$ °C.

$$H_2O_2 + {}^{\bullet}OH \rightarrow H_2O + {}^{\bullet}OOH \quad (7)$$

$$HO_2^{\bullet} + {}^{\bullet}OH \rightarrow H_2O + O_2 \quad (8)$$

Catalyst dosage played a crucial role in ERY degradation. As depicted in Fig. 10a, when the dosage of GO/MIL-100(Fe)@Fe_3O_4 increased from 0.05 g L^{-1} to 0.1 g L^{-1}, ERY degradation efficiency increased, and the kinetic constant increased from 0.0302 min^{-1} to 0.0575 min^{-1}. This was attributed to the fact that the appropriate amount of catalyst provided sufficient active sites, which was favorable for ERY degradation. However, when the catalyst dosage continued to increase to 0.4 g L^{-1}, the ERY degradation efficiency decreased, and the related kinetic constant decreased to 0.0325 min^{-1}. Excessive catalyst increased the turbidity of the

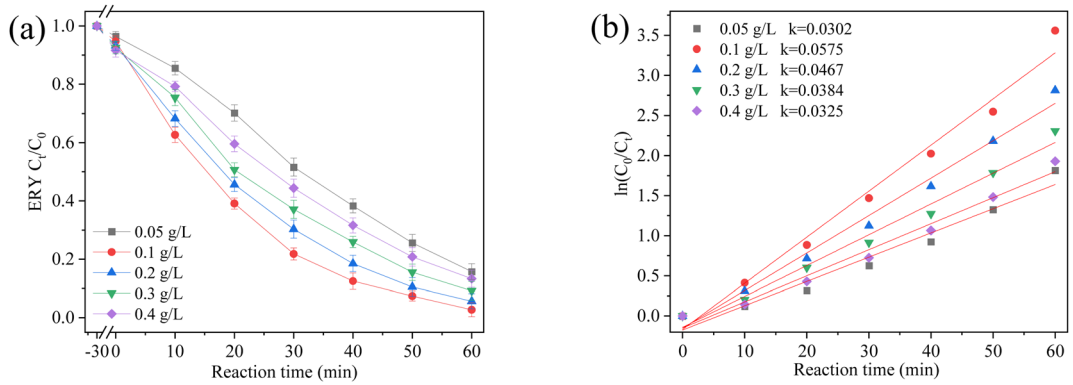

Fig. 10 Effect of the catalyst dosage on the photo-Fenton degradation of ERY (a), and kinetic analysis of the degradation of ERY at different catalyst dosages (pseudo-first-order kinetics model) (b). pH = 4.03, $[H_2O_2]_0 = 10$ mmol L^{-1}, $[ERY]_0 = 0.1$ mmol L^{-1}, $T = 30$ °C.

ERY suspension, leading to decreased transparency of the solution, influencing the light absorption by the catalyst, and thus hindering the photo-Fenton reaction process.[41]

In natural water, the coexisting natural organic matter (*e.g.*, humic acid, HA) and inorganic anions (HCO_3^-, $H_2PO_4^-$, Cl^-, SO_4^{2-}, NO_3^-) could influence interfacial reactions related to reactive radicals. The influences of HA and common anions on the degradation of ERY were analyzed using simulated wastewater (Fig. 11a and b). The ERY degradation efficiency decreased from 97.3% to 76.5%, and the related kinetic constant (k) decreased from 0.0575 min^{-1} to 0.0240 min^{-1}. HA inhibited degradation by complexing iron species, scavenging radicals and competing with ERY molecules for adsorption sites.[42] SO_4^{2-} and NO_3^- had little influence on ERY degradation. Cl^-, $H_2PO_4^-$ and HCO_3^- showed obvious inhibition of ERY degradation, because Cl^-, $H_2PO_4^-$ and HCO_3^- in solution can react with free radicals. Notably, HCO_3^- can react with Fe species. It can also act as a scavenger for reactive oxygen species, generating less reactive species, such as $HCO_3^{\bullet}$ and $CO_3^{\bullet-}$.[43] The removal efficiency decreased from 97.3% to 63.9%, and the related kinetic constant (k) decreased from 0.0575 min^{-1} to 0.0174 min^{-1}. $H_2PO_4^-$ led to a reduction in ERY removal efficiency, from 97.3% to 72.4%, and the related kinetic constant (k) decreased from 0.0575 min^{-1} to 0.0198 min^{-1}. $H_2PO_4^-$ may react with highly reactive free radicals to generate less oxidative $H_2PO_4^{\bullet}$, and Fe–O may also accumulate on the catalyst surface and react with free H^+ to generate Fe–OH, which can react with $H_2PO_4^-$ to form inner complexes (such as $FeH_2PO_4^+$/$FeHPO_4$), thus covering surface active sites.[43] Cl^- led to a reduction in ERY degradation efficiency, from 97.3% to 76.5%, and the kinetic constant (k) decreased from 0.0575 min^{-1} to 0.0216 min^{-1}. Cl^- can scavenge highly reactive free radicals to generate less reactive radicals (such as $Cl^{\bullet}$ and $Cl_2^{\bullet-}$).[42] SO_4^{2-} and NO_3^- showed minimal interaction with electrons, ROS and Fe species. The slight negative influence of SO_4^{2-} and NO_3^- on ERY degradation may be due to competition for reaction sites, but it was negligible.[43]

3.4. Stability of GO/MIL-100(Fe)@Fe_3O_4

The stability of a catalyst is crucial for the practical application of photo-Fenton. The stability of GO/MIL-100(Fe)@Fe_3O_4 was estimated using recycling experiments. As can be seen in Fig. 12, after four cycles of reactions, the ERY and corresponding TOC removal efficiencies were 90.8% and 25.9%, respectively, suggesting that ERY was partially decomposed into smaller molecules by photo-Fenton degradation. ERY was not completely mineralized into CO_2. According to previous studies, heterocyclic by-products, aromatic methyl ester derivatives and tertiary aliphatic amines have been detected during ERY Fenton degradation. The by-products are generated by the cleavage of multiple C–C bonds of ERY, followed by internal cyclization to generate a heterocyclic and aromatic structure.[44] Some short-chain aliphatic carboxylic acids, such as maleic, fumaric, oxamic, oxalic and formic acids, have also been detected.[44] Further research is required to analyze the harmlessness of the remaining TOC to living beings. After four cycles, an insignificant decrease in ERY degradation efficiency and TOC removal was found (Fig. 12a); the iron leaching was at a low level (Fig. 12b); and the magnetic properties (Fig. 12c) and crystal structure (Fig. 12d) of the catalyst had not changed very much, indicating the good stability of GO/MIL-100(Fe)@Fe_3O_4 and that it would be an excellent photo-Fenton catalyst for ERY treatment in water.

3.5. Analyses of reactive oxidizing species

To further verify the main active species in the reactions, free radical capture experiments were performed using 20 mmol L^{-1} tertiary butanol (TBA), silver nitrate ($AgNO_3$), ammonium oxalate (AO), and *p*-benzoquinone (BQ), as capture agents for $^{\bullet}OH$, e^-, h^+ and $^{\bullet}O_2^-$, respectively. Fig. 13a obviously indicates that after adding TBA and AO, ERY removal efficiency decreased from 97.3% to 18.4% and 10.6%, respectively, and the related kinetic constants also decreased significantly (Fig. 13b), indicating that $^{\bullet}OH$ and h^+ played a dominant role in the removal of ERY. After adding $AgNO_3$ and BQ, the interference effect on ERY removal was very low, suggesting that $^{\bullet}O_2^-$ was a minor active species for ERY degradation, while e^- made the weakest contribution to ERY degradation.

3.6. Possible degradation mechanism

Based on ERY degradation experiments, the degradation efficiency of different systems ranked from highest to lowest was:

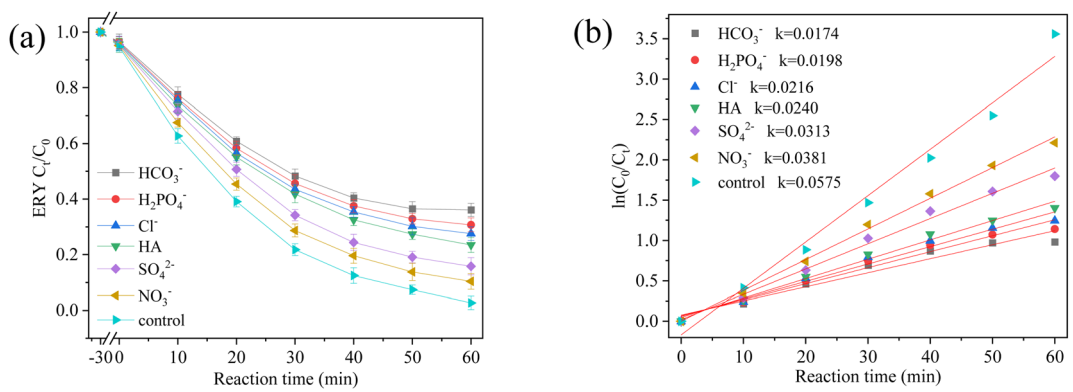

Fig. 11 Effect of coexisting HA and anions on the photo-Fenton degradation of ERY (a), and kinetic analysis of the degradation of ERY with coexisting HA and anions (pseudo-first-order kinetics model) (b). pH = 4.03, $[catalyst]_0$ = 0.1 g L^{-1}, $[H_2O_2]_0$ = 10 mmol L^{-1}, $[ERY]_0$ = 0.1 mmol L^{-1}, [HA] = 10 mg L^{-1}, [anion] = 10 mg L^{-1}, T = 30 °C.

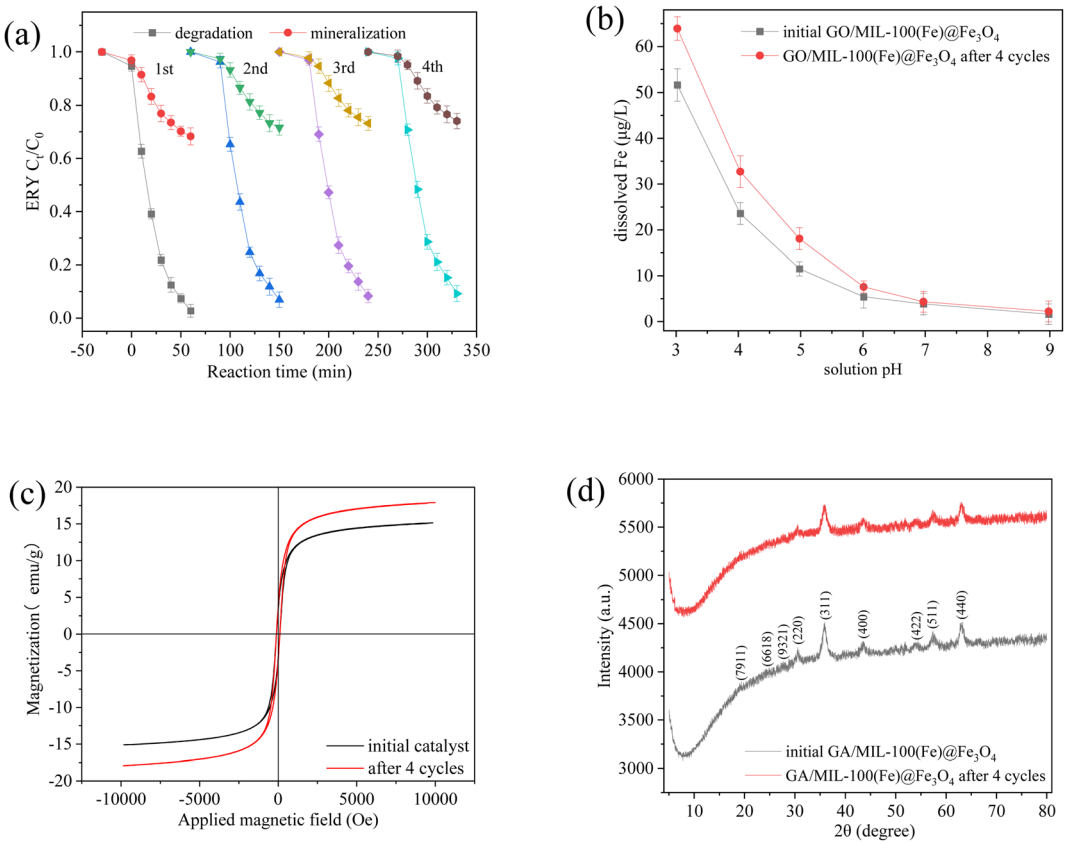

Fig. 12 Cycles of ERY degradation in the photo-Fenton system (a), leaching of Fe during the 1st cycle and 4th cycle (b), magnetic hysteresis loop at 298 K (c) and XRD patterns (d) of initial GO/MIL-100(Fe)@Fe_3O_4 and a sample after 4 cycles under the optimum conditions. pH = 4.03, $[H_2O_2]_0$ = 10 mmol L^{-1}, [catalyst]$_0$ = 0.1 g L^{-1}, [ERY]$_0$ = 0.1 mmol L^{-1}, T = 30 °C.

GO/MIL-100(Fe)@Fe_3O_4 + H_2O_2 + vis > MIL-100(Fe)@Fe_3O_4 + H_2O_2 + vis > MIL-100(Fe) + H_2O_2 + vis > GO@Fe_3O_4 + H_2O_2 + vis > GO/MIL-100(Fe)@Fe_3O_4 + H_2O_2 > Fe_3O_4 + H_2O_2 + vis > GO/MIL-100(Fe)@Fe_3O_4 + vis. GO/MIL-100(Fe)@Fe_3O_4 showed the highest degradation efficiency under the same initial conditions. Visible light significantly promoted the degradation of ERY, suggesting the synergistic effect of the visible-light-induced reaction and the Fenton reaction. A possible mechanism for photo-Fenton degradation of ERY by GO/MIL-100(Fe)@Fe_3O_4 was proposed (Fig. 14), and the reaction equations can be seen in the following equations.[45]

In the visible-light-induced reaction, the Fe–O cluster in MIL-100(Fe) was excited by visible light,[45] and photogenerated electrons (e^-) and photogenerated holes (h^+) were generated over the MIL-100(Fe) surface (eqn (9)). Subsequently, as the level of the CB of Fe_3O_4 NPs was lower than that of MIL-

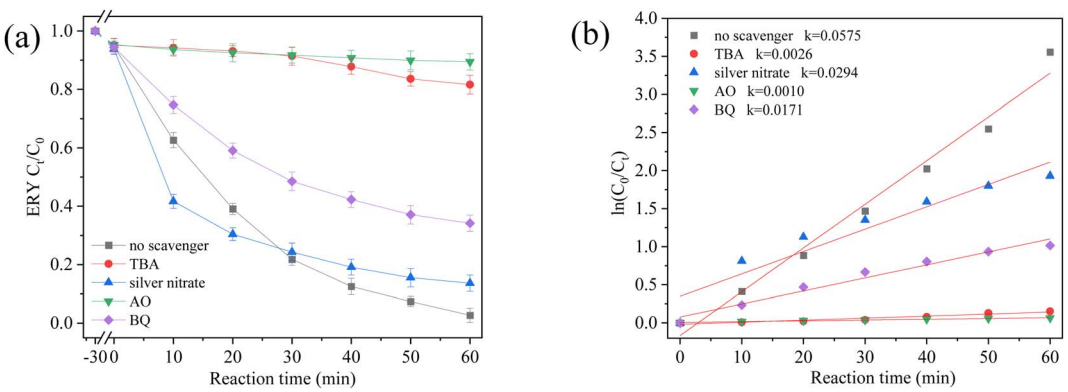

Fig. 13 Effect of radical scavengers on the photo-Fenton degradation of ERY (a), and kinetic analysis of the degradation of ERY with different radical scavengers (pseudo-first-order kinetics model) (b). pH = 4.03, $[H_2O_2]_0$ = 10 mmol L^{-1}, [catalyst]$_0$ = 0.1 g L^{-1}, [ERY]$_0$ = 0.1 mmol L^{-1}, T = 30 °C.

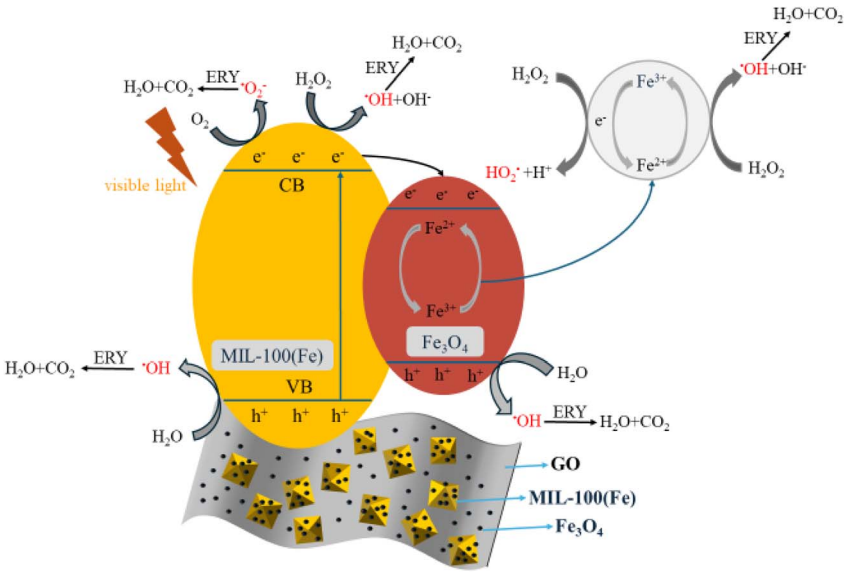

Fig. 14 The proposed degradation mechanism of ERY in the photo-Fenton system over GO/MIL-100(Fe)@Fe_3O_4.

100(Fe), the photogenerated electrons from MIL-100(Fe) were transferred to the surface of the Fe_3O_4 NPs, hindering the recombination of photogenerated e^-–h^+ pairs.[45] Then photogenerated electrons and holes could be delivered to H_2O_2, O_2 and Fe_3O_4 NPs, where the electrons reacted with H_2O_2 and O_2 to form $^{\cdot}OH$ and $^{\cdot}O_2^-$ (eqn (10) and (11)),[46] and the holes reacted with H_2O to form $^{\cdot}OH$ (eqn (12)), while H_2O_2 can also form $^{\cdot}OH$ under light irradiation (eqn (5)). GO may act as a charge transfer bridge, facilitating the separation of e^-–h^+ and the migration of photogenerated electrons from MIL-100(Fe) to Fe_3O_4 NPs. The migration of electrons was in the opposite direction to that of holes, which was favorable for hindering e^-–h^+ recombination, thus improving the utilization efficiency of e^- and h^+. Furthermore, holes with strong oxidation capacity could also attack ERY, and ERY could be decomposed into small molecules.

In the Fenton reaction, Fe_3O_4 NPs acted as nuclei to provide Fe^{2+}, which reacted with H_2O_2 to produce $^{\cdot}OH$ and Fe^{3+}, and Fe^{3+} was also slowly reduced to Fe^{2+}, which could continuously generate $^{\cdot}OH$. When Fe_3O_4 NPs were bound to MIL-100(Fe), Fe_3O_4 NPs acted as electron acceptors, promoting the Fe^{2+}/Fe^{3+} cycle (eqn (13)). GO acted as an electron transfer channel, where photogenerated electrons were immediately transferred to the surface of Fe_3O_4 NPs through GO, thus accelerating Fe^{3+} in GO/MIL-100(Fe)@Fe_3O_4 being converted to Fe^{2+} (eqn (13)). Meanwhile, the added H_2O_2 could capture electrons from the visible-light-induced reaction to produce $^{\cdot}OH$, and Fe^{3+} in Fe_3O_4 NPs could also be converted to Fe^{2+} by the electrons. The generated Fe^{2+} react with H_2O_2 in the Fenton reaction, accelerating the Fe^{2+}/Fe^{3+} cycle (eqn (1) and (2)). Finally, the generated h^+, $^{\cdot}OH$ and $^{\cdot}O_2^-$ participated as active species in the degradation of ERY (eqn (14)). In this way, MIL-100(Fe), Fe_3O_4 NPs and GO in GO/MIL-100(Fe)@Fe_3O_4 showed synergistic effects, exhibiting excellent catalytic activity for the degradation of ERY.

$$\text{GO/MIL-100(Fe)@}Fe_3O_4 + h\nu \rightarrow \text{GO/MIL-100(Fe)@}Fe_3O_4\ (e^-\text{–}h^+) \quad (9)$$

$$e^- \text{ (MIL-100(Fe))} + O_2 \rightarrow {}^{\cdot}O_2^- \quad (10)$$

$$e^- \text{ (MIL-100(Fe))} + H_2O_2 \rightarrow {}^{\cdot}OH + OH^- \quad (11)$$

$$h^+ + H_2O \rightarrow {}^{\cdot}OH + H^+ \quad (12)$$

$$e^- + Fe^{3+} \rightarrow Fe^{2+} \quad (13)$$

$$h^+/{}^{\cdot}OH/{}^{\cdot}O_2^- + \text{ERY} \rightarrow \text{intermediates} \rightarrow H_2O + CO_2 \quad (14)$$

4. Conclusions

In this study, GO/MIL-100(Fe)@Fe_3O_4 was synthesized *via* an *in situ* growth method and showed excellent photo-Fenton catalytic performance for ERY degradation over a wide pH range. ERY degradation was conducted under different reaction conditions. The degradation efficiency of ERY in the GO/MIL-100(Fe)@Fe_3O_4 + H_2O_2 + vis system achieved 97.3% within 60 min. Free radical quenching experiments indicated that various active species, such as h^+, $^{\cdot}OH$, $^{\cdot}O_2^-$ and e^-, participated in ERY degradation, but h^+ and $^{\cdot}OH$ played a dominant role. GO/MIL-100(Fe)@Fe_3O_4 not only showed excellent catalytic activity, but also showed good stability: after four cycles, the degradation efficiency for ERY still remained above 85%. The excellent catalytic activity of GO/MIL-100(Fe)@Fe_3O_4 could be ascribed mainly to the following: (1) an improvement in charge distribution and acceleration of the Fe^{3+}/Fe^{2+} cycle derived from the synergistic effects between Fe_3O_4 NPs and MIL-100(Fe); (2) GO acting as an electron transfer channel facilitated the transfer of photogenerated electrons over MIL-100(Fe), hindered the recombination of photogenerated carriers, and accelerated the Fe^{3+}/Fe^{2+} cycle; and (3) multiple

active species participated in ERY degradation. The results indicated that GO/MIL-100(Fe)@Fe_3O_4 would be an excellent heterogeneous photo-Fenton catalyst for wastewater treatment.

Author contributions

Lian Yu: writing – original draft, methodology, investigation, formal analysis. Baozi Lu: methodology, investigation. Zhen Liang: writing – review and editing, methodology, formal analysis. Dabin Wang: writing – review and editing, investigation. Jiarui Lu: data curation, methodology. Fengyi Wei: methodology, formal analysis. Cunzhen Liang: project administration, funding acquisition, conceptualization.

Conflicts of interest

The authors declare that they have no known competing financial interests or personal relationships that could have appeared to influence the work reported in this paper.

Data availability

All data supporting the findings of this study are included in the main manuscript.

Supplementary information (SI) is available. See DOI: https://doi.org/10.1039/d5ra06917c.

Acknowledgements

This work was supported by the Zhiyuan Science Foundation of BIPT (Project No. 2023004) and the National College Students Innovation and Entrepreneurship Training Program (Grant No. 2025J00015, 2025J00016 and 2020J00184).

References

1 M. Sharma, A. Bains, K. Sridhar, P. Chawla and M. Sharma, *Food Chem. Toxicol.*, 2024, **193**, 115038.
2 V. Meena, D. Swami, A. Chandel, N. Joshi and S. O. Prasher, *J. Hazard. Mater.*, 2025, **483**, 136541.
3 L. O. Omuferen, B. Maseko and J. O. Olowoyo, *Environ. Monit. Assess.*, 2022, **194**, 306.
4 J. P. Li, W. Li, K. Liu, Y. H. Guo, C. Ding, J. G. Han and P. P. Li, *J. Hazard. Mater.*, 2022, **439**, 129628.
5 D. T. Dou, Y. D. Zhao, C. Y. Yang, J. J. Deng, L. S. Lian and T. S. Zhou, *Sep. Purif. Technol.*, 2025, **366**, 132823.
6 X. G. Jin, H. Y. Lim, Q. Wang, R. Jia, X. H. Ma, Z. L. Xu and C. Y. Tang, *Environ. Sci. Technol.*, 2025, **59**(29), 15538–15546.
7 H. J. Cao, J. C. Liu, W. You, G. H. Lu, Y. P. Li, J. Hou and P. Gao, *J. Environ. Manage.*, 2025, **388**, 125965.
8 K. B. Bodle and C. M. Kirkland, *Int. Biodeterior. Biodegrad.*, 2025, **202**, 106081.
9 K. McCorquodale-Bauer, R. Grosshans, F. Zvomuya and N. Cicek, *Sci. Total Environ.*, 2023, **870**, 161876.
10 Y. Zhu, J. Zhu, H. ShenTu, Y. Wei, J. Wei, L. Lei, Y. Li, T. Yu, Z. Li, Y. Hou and B. Yang, *Appl. Catal., B*, 2023, **334**, 122824.
11 Y. Ren, J. Zhang, C. Ji, S. Wang, L. Lv and W. Zhang, *Sci. Total Environ.*, 2022, **809**, 152201.
12 E. Brillas, *J. Environ. Chem. Eng.*, 2025, **13**, 115443.
13 H. R. Ahmed, *Sep. Purif. Technol.*, 2025, **374**, 133670.
14 Y. Ren, M. Shi, W. Zhang, D. D. Dionysiou, J. Lu, C. Shan, Y. Zhang, L. Lv and B. Pan, *Environ. Sci. Technol.*, 2020, **54**, 5258–5267.
15 A. Soufi, H. Hajjaoui, W. Boumya, A. Elmouwahidi, E. Baillón-García, M. Abdennouri and N. Barka, *J. Environ. Manage.*, 2024, **367**, 121971.
16 W. He, Z. Li, S. Lv, M. Niu, W. Zhou, J. Li, R. Lu, H. Gao, C. Pan and S. Zhang, *Chem. Eng. J.*, 2021, **409**, 128274.
17 C. Wu, T. Guo, Y. Chen, Q. Tian, Y. Zhang, Z. Huang, H. Hu and T. Gan, *Sep. Purif. Technol.*, 2024, **329**, 125174.
18 Z. C. Yi, X. Y. Yang, Y. Liang, F. Chapelin and S. Tong, *Small*, 2023, **20**(6), 2305974.
19 H. Zhou, H. Zhang, Y. He, B. Huang, C. Zhou, G. Yao and B. Lai, *Appl. Catal., B*, 2021, **286**, 119900.
20 L. Li, M. Cheng, E. Almatrafi, L. Qin, S. Liu, H. Yi, L. Yang, Z. Chen, D. Ma, M. Zhang, X. Zhou, F. Xu, C. Zhou, L. Tang, G. Zeng and C. Lai, *J. Hazard. Mater.*, 2023, **457**, 131800.
21 B. L. Hou, J. Y. Liu, J. P. Tang, Z. Li, J. K. Shu, Z. H. Wang, B. Z. Ren, R. J. Deng, Y. Liu and A. Hursthouse, *J. Environ. Chem. Eng.*, 2025, **13**, 115126.
22 V. T. Le, V. D. Doan, T. T. N. Le, M. U. Dao, T. T. T. Vo, H. H. Do, D. Q. Viet and V. A. Tran, *Mater. Lett.*, 2021, **283**, 128749.
23 R. Zhao, X. W. Yang, Q. Liu, H. X. Zhao, H. Zhan, F. Y. Chen and Z. R. Shen, *Sep. Purif. Technol.*, 2025, **363**, 132213.
24 X. Liang, L. Li, Y. Wu, F. Liu, Y. Wang and Y. Wu, *J. Alloys Compd.*, 2025, **1038**, 182610.
25 X. Liang, L. Li, Y. Wu, F. Liu and Y. Wang, *Appl. Surf. Sci.*, 2025, **697**, 163029.
26 Q. Gong, Y. Liu and Z. Dang, *J. Hazard. Mater.*, 2019, **371**, 677–686.
27 Z. Fang, M. Y. Li, T. R. Li, C. R. Zhao, H. Y. Liu, M. X. Huo and S. S. Dong, *Sep. Purif. Technol.*, 2025, **366**, 132751.
28 Y. Zhang, F. Liu, Z. Yang, J. Qian and B. Pan, *Nano Res.*, 2021, **14**, 2383–2389.
29 J. Zhu, J. Ma, L. Liu, S. Zhang, L. Zhao, H. Jin and K. Zhang, *Environ. Sci. Pollut. Res.*, 2023, **30**, 7207–7217.
30 M. D. Yu, D. W. Huang, X. T. Sun, X. F. Chen, L. W. Yang and F. He, *J. Environ. Chem. Eng.*, 2025, **13**, 116114.
31 M. Liu, Y. Liu, X. Liu, C. Chu, D. Yao and S. Mao, *Sep. Purif. Technol.*, 2022, **301**, 121967.
32 B. M. Esteves, S. Morales-Torres, F. J. Maldonado-Hódar and L. M. Madeira, *J. Water Process Eng.*, 2024, **58**, 104772.
33 W. Zhang, Y. Z. Zhang and J. M. Yang, *J. Mol. Struct.*, 2022, **1265**, 133365.
34 X. Zhang, Z. Yao, Y. Zhou, Z. Zhang, G. Lu and Z. Jiang, *Chem. Eng. J.*, 2021, **411**, 128535.
35 J. Scaria and P. V. Nidheesh, *Environ. Sci.: Water Res. Technol.*, 2022, **8**, 1261–1276.
36 Z. Ren, F. Chen, K. Wen and J. Lu, *J. Photochem. Photobiol., A*, 2020, **389**, 112217.

37 Y. Wei, Z. Fu, Y. Meng, C. Li, F. Yin, X. Wang, C. Zhang, L. Guo and S. Sun, *Int. J. Coal Sci. Technol.*, 2024, **11**, 42.
38 F. Gamboa-Savoy, C. Onfray, J. Correa-Puerta, D. P. Pabba, N. Hassan and A. Thiam, *Appl. Catal. O: Open*, 2025, **206**, 207063.
39 L. He, J. Zhou, D. Liu, Y. Wen and Y. Gan, *Mater. Sci. Semicond. Process.*, 2024, **172**, 108050.
40 J. Guo, H. Jia, A. Zhang, Z. Pei, M. Luo, J. Xue, Q. Shen, X. Liu and B. Xu, *Sep. Purif. Technol.*, 2021, **262**, 118334.
41 H. Sun, T. Zhou, J. Kang, Y. Zhao, Y. Zhang, T. Wang and X. Yin, *Sep. Purif. Technol.*, 2022, **299**, 121771.
42 B. Ran, J. Pan, Q. Yan, Q. Wu, R. Zhuang, Y. Zhou, Z. Zhao and X. Zhang, *Diamond Relat. Mater.*, 2024, **149**, 111545.
43 H. Fakhri, M. Farzadkia, R. Boukherroub, V. Srivastava and M. Sillanpää, *Sol. Energy*, 2020, **208**, 990–1000.
44 T. Pérez, I. Sirés, E. Brillas and J. L. Nava, *Electrochim. Acta*, 2017, **228**, 45–56.
45 J. Zhao, J. Liu, Y. Han, C. Lu, J. Li, W. Li, H. Xu, J. Gao and A. Li, *Water Res.*, 2026, **288**, 124525.
46 Y. Fu, Y. Yi, Y. Wang and Z. Diao, *J. Water Process Eng.*, 2025, **78**, 108636.